RESEARCH ARTICLE

Adaptive Frequency Control Strategy for PMSG-Based Wind Turbines With Improved Rotor Speed Recovery

DUC-TUNG TRINH[1], (Graduate Student Member, IEEE), **YUAN-KANG WU**[1], (Member, IEEE), **AND MANH-HAI PHAM**[2], (Member, IEEE)

[1]Department of Electrical Engineering, National Chung Cheng University, Chiayi 62102, Taiwan
[2]Department of Energy Technology, Electric Power University, Hanoi 10000, Vietnam

Corresponding author: Manh-Hai Pham (haipm@epu.edu.vn)

ABSTRACT In modern power systems, the increasing penetration of renewable energy resources has reduced frequency stability. Consequently, wind turbines (WTs) are expected to participate in frequency regulation. By integrating the electrostatic energy stored in the DC capacitor with the kinetic energy stored in the rotating mass of the WT, an advanced control method is implemented to facilitate frequency regulation. However, previous studies have mainly concentrated on frequency control using WTs but ignored the rotor speed recovery of WT. Therefore, this work proposes a novel control strategy that separates the operating mode of a WT into two distinct states: the frequency support and the recovery of rotation speed stages. The proposed method improves the recovery process for rotor speeds after a WT participates in frequency support, returning the WT quickly to its normal operation to reduce wind energy loss. Furthermore, a new adaptive DC virtual inertia (DVIC) coefficient that utilizes real-time DC voltage to adjust the DVIC's output smoothly is proposed. The proposed strategy is compared with other mature control strategies and implemented in PSCAD/EMTDC to verify their effectiveness and robustness. The simulation results demonstrate that the proposed method outperforms other mature methods because it reduces wind energy loss by at least 15 % when WTs participate in the frequency support process.

INDEX TERMS Frequency regulation, rotor speed recovery, PMSG, inertia and droop control, wind generation.

ABBREVIATIONS

PMSG	Permanent Magnet Synchronous Generator.
WT	Wind Turbine.
MPPT	Maximum Power Point Tracking.
FN	Frequency Nadir.
FS	Frequency Support.
RS	Recovery of Rotation Speed.
EE	Electrostatic Energy.
KE	Kinetic Energy.
SIC	Stepwise Inertial Control.
SG	Synchronous Generators.
RVIC	Rotor Virtual Inertia Control.
ROCOF	Rate of Change of Frequency.
DVIC	DC Virtual Inertia Control.
RSC	Rotor Side Converter.
GSC	Grid Side Converter.
PWM	Pulse Width Modulation.
RES	Renewable Energy Source.
PCC	Point of Common Coupling.

The associate editor coordinating the review of this manuscript and approving it for publication was Fabio Mottola.

I. INTRODUCTION

With the high penetration of wind power in the power grids, the system inertia is reduced, which causes the frequency stability to become more volatile and unpredictable.

Contrary to conventional power plants, the permanent magnet synchronous generator (PMSG)-based wind turbine (WT) utilizes a maximum power point tracking (MPPT) algorithm to maximize wind energy harvesting [1], [2]. The use of back-to-back converters causes the WTs to decouple from the power system, which makes them incapable of directly responding to any frequency disturbance in an AC system [3]. Thus, the frequency nadir (FN) could become lower, and the frequency deviation could be large, causing a load shedding and even a blackout [4], [5].

To address these challenges, WTs are anticipated to participate in frequency regulation. The frequency regulation by WTs typically divides into two stages: the frequency support (FS) and the recovery of rotation speed (RS) [6], [7], [8]. WTs can contribute to frequency regulation by utilizing the DC capacitor's stored electrostatic energy (EE) and the kinetic energy (KE) stored in the rotating mass. The inertia control approach uses the spinning KE stored in the rotating mass of WTs to participate in frequency support during sudden load changes or disturbances. Two widely discussed inertial control techniques are temporary and persistent energy reserves. Persistent energy reserves rely on de-loading through rotor speed control and pitch angle control approach [9], [10]. The active and passive reactions are advanced methods that enable WT to store energy reserves temporarily. More precisely, the stepwise inertial control (SIC) and fast power reserve will actively engage in frequency management, as stated in [11], [12], [13], [14], [15], [16], [17], [18], [19], and [20]. In contrast with active response, passive response uses inertia and droop control to quickly respond to the frequency event by detecting the fault in the power system [21], [22], [23], [24], [25], [26], [27], [28], [29], [30], [31], [32], [33], [34].

With the deloading method, WT will shift the MPPT operating point away from the optimal one and sacrifice much-captured energy for system support [9], [10]. The response speed is relatively slow due to the mechanical regulation of pitch angle, leading to decreased speed response. In addition, frequent blade pitching activation for system support will make WT more fatigued and mechanically stressed. The SIC method is an advanced strategy for improving the frequency support impact of WTs. It achieves this using a frequency-independent approach, as demonstrated in [11], [12], [13], [14], and [15]. To recover the rotor speed after providing frequency support, SIC reduces the WT output in a step-like manner [14], [16] or in a ramp manner [17], [18]. However, the former control method causes a second frequency dip (SFD) due to the rapid output reduction. The over-production strategy to allow rotor speed recovery was proposed in [19] and [20] to ensure the rotor speed does not over-decelerate.

The frequency-based inertia control mimics the inertial response of synchronous generators (SGs), in which the rotor virtual inertia control (RVIC) employs rate of change of frequency (ROCOF), and the droop control uses frequency deviation as the input signal [21], [22], [23], [24]. The
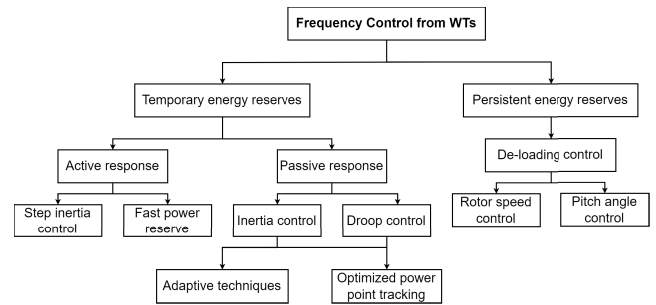

FIGURE 1. Categorization of frequency control from WTs.

RVIC mainly affects the initial transient frequency when a disturbance occurs, while the droop control activates during the remaining time of the FS state. Thus, the droop coefficient significantly influences wind energy production. As a result, the droop control using a fixed droop coefficient is unsuitable for all operating conditions. The authors in [25] introduced the time-varying virtual inertia and droop coefficients, which help raise the FN compared to a constant coefficient. An adaptive droop control based on rotor speed was proposed in [26], which performs better when WTs participate in frequency regulation under different wind speeds. Based on the above literature reviews, typical frequency control methods of WTs can be summarized in Fig. 1.

The DC virtual inertia control (DVIC) utilizes the EE stored in the DC capacitor to provide emulated inertia for power systems [27]. However, a tiny capacitance at the DC-link results in less energy stored in the capacitor. The supercapacitor connected to the DC-link can improve WT frequency support capability, which was investigated in [28], [29], [30], and [31]. A method for controlling synthetic inertia in DFIG WTs utilizing lithium-ion supercapacitors is proposed in [28]. The supercapacitor installed at the DC-link offers DVIC and short-term primary frequency regulation support, as investigated in [31]. Using a supercapacitor, however, might increase the converter's volume, cost, and complexity of the control algorithm.

The coordination between the frequency-based inertia control and the DVIC is an appropriate solution for WTs to enhance their frequency-support capability. The simultaneous use of these strategies improves WT frequency-support ability, which is discussed in [27] and [32]. Nevertheless, the simultaneous approach leads to the unnecessary loss of wind energy. A cascading strategy was developed to select the priority between the DVIC and frequency-based inertia control strategies [33]. It initially utilizes the whole EE in the DC capacitor and subsequently harnesses the rotational KE of WTs to participate in frequency regulation. Therefore, the cascading method ensures that less wind energy is wasted. However, switching between the two controls will continuously happen if the DC voltage fluctuates around the boundary point. The authors in [34] introduced a time-sharing frequency coordinated control (TFCC) technique. This strategy employs a frequency deadband to determine the priority between the DVIC and frequency-based inertia controllers.

The TFCC strategy can avoid the disadvantages of the cascading strategy. The authors in [32], [33], and [34] utilized a constant DC virtual coefficient for the DVIC, disregarding the real-time DC voltage value. Meanwhile, the DC voltage reflects the capacity to generate active power at the output of the DVIC controller. Consequently, the additional power generated by the DVIC controller abruptly reverts to zero when the DC voltage exceeds the allowable operation range. In addition, the papers [27], [28], [29], [30], [31], [32], [33], [34] used coordinated strategies for both the FS and RS processes when WTs contributed to frequency regulation. Instead of using the rotor speed information, these strategies use the frequency deviation as a controller's input for the RS strategy to return the WTs to a nominal operation. It does not optimize the recovery process of WTs. Moreover, when the frequency deviation returns to the deadband in the RS state, the algorithm automatically turns off the frequency-based inertia controller. This forces the additional power output to zero and causes the power reference value of WTs to return to the MPPT operating point suddenly.

To overcome these problems, this work proposes a new control strategy that divides the frequency regulation into two stages: the first stage implements FS using a coordinate strategy, while the second stage provides a novel RS strategy to determine the power reference value for the RS process. The main contributions of this work are summarized as follows:

1) This work proposes a new frequency regulation strategy that automatically switches the operation between FS and RS based on the sign of derivative rotor speed during an accident. A corresponding control strategy for FS or RS is applied at each stage. The DVIC and frequency-based inertia control strategies are adopted to provide frequency support in the FS state.

2) This work presented a novel power reference for the RS state based on the relationship between the MPPT curve and the mechanical power. As a result, the loss of wind energy is minimized. Additionally, it avoids the active power reference of WTs suddenly returning to the MPPT operating point once the frequency-based inertia controller is disabled.

3) A novel DC adaptive virtual inertia coefficient has been developed concerning the real-time DC voltage. The proposed method smoothly returns the DVIC controller's output to zero instead of a sudden change in the output if a fixed coefficient is employed.

This manuscript is structured as follows: Section II presents the PMSG-based WT model. The frequency-based inertia control and DC virtual inertia control are discussed in section III. Section IV proposes a novel adaptive DC virtual coefficient and power command setting method for WTs during the RS operating state. Section V contains the simulation results on a test system. Section VI draws the conclusions.
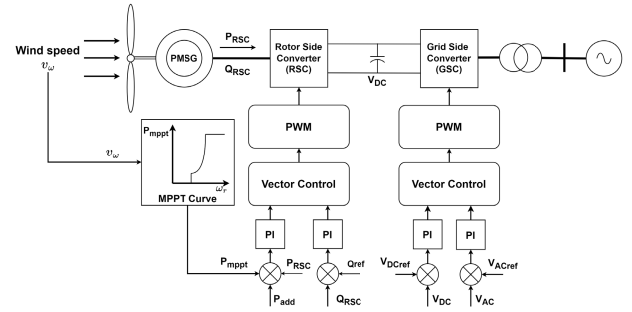

FIGURE 2. Control diagram of a PSMG-based WT.

II. PMSG-BASED WIND TURBINE MODEL

Fig. 2 depicts the schematic diagram of the PMSG-based WT system, in which the generation is connected via a full-capacity power converter [35]. The rotor-side converter (RSC) aims to control the optimal active power output by tracking the active power reference using the MPPT algorithm and controlling the reactive power exchange between the induction generator and the power grid [21], [33]. The grid-side converter (GSC) fulfills two primary functions: firstly, it controls the DC voltage to ensure a balance of active power between RSC and GSC, and secondly, it maintains a specified magnitude of the WT voltage at the point of common coupling (PCC) [35], [36]. The voltage source converters at RSC and GSC produce a voltage waveform that may be flexibly controlled in amplitude and phase angle using the pulse width modulation (PWM) technique. The detailed control scheme of the power electronic converter and control algorithm are presented in [37] and [38]. The mechanical power P_ω extracted from wind energy is given in (1).

$$P_\omega = \frac{\rho}{2}\pi R^2 v_\omega^3 C_p(\lambda, \beta). \tag{1}$$

where ρ is the air density, R is the rotor blade radius, v_ω is the wind speed, λ is the tip speed ratio, β is the pitch angle, and C_p is the power coefficient. The power coefficient is a function between λ and β, which can be given in [34] and [39].

$$C_p = 0.5176\left(\frac{116}{\lambda_i} - 0.4\beta - 5\right)e^{-\frac{21}{\lambda_i}} + 0.0068\lambda. \tag{2}$$

where the tip speed ratio can be determined as follows:

$$\lambda = \frac{\omega_r R}{v_\omega}. \tag{3}$$

where ω_r is the rotor speed. The pitch angle is normally kept zero when the wind speed is below the rated value. Hence, C_p is the function of λ only and reaches the maximum $C_{p,max}$ at the optimal tip speed ratio λ_{opt} as described in (4) [33], [34].

$$P_{mppt} = \frac{\pi\rho R^5 C_{p,max}}{2\lambda_{opt}^3}\omega_r^3 = k_{opt}\omega_r^3. \tag{4}$$

where P_{mppt} is the active power reference determined by the MPPT algorithm, and k_{opt} is the MPPT curve coefficient. The relationship between the active power of WT and wind
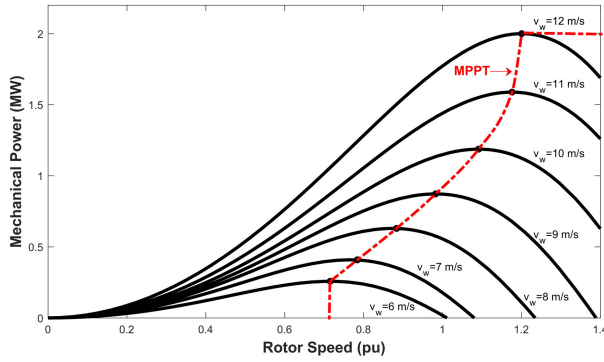
FIGURE 3. WT power-speed characteristics and maximum power point operation.

FIGURE 4. DC virtual inertia control strategy.

TABLE 1. The lookup table of each point on the power-speed curve.

Points	Wind speed (m/s)	Mechanical Power (MW)
1	6	0.2578
2	7	0.4088
3	8	0.6298
4	9	0.8725
5	10	1.1874
6	11	1.5886
7	12	2.0
8	13	2.0
9	14	2.0

speed is extensively discussed in [40] and [41]. The operation characteristics of WT as a function of rotor speed ω_r and the mechanical power P_ω are presented in Fig. 3, while the corresponding relationship between them is shown in Table 1. The power reference P_{mppt} compares with the measured power P_{RSC} from the generator to produce the control signals for the power converter, as shown in Fig. 2.

III. VIRTUAL INERTIA CONTROL STRATEGY

A. FREQUENCY-BASED INERTIA CONTROL

A typical frequency-based inertia control contains RVIC and droop control. Generally, the RVIC strategy uses the ROCOF as the input signal to simulate the inertial response of a SG [22]. The additional power P_{VIC} is proportional to ROCOF, which can be determined by:

$$P_{VIC} = -2H_{VIC}\frac{d\Delta f}{dt}. \tag{5}$$

where H_{VIC} is the virtual inertia time constant of the RVIC, and Δf refers to the measured frequency deviation. The droop control strategy output power is proportional to the system frequency deviation Δf, which can be given in (6).

$$P_D = -K_D\Delta f. \tag{6}$$

where K_D is the droop coefficient. Under normal conditions, a WT will use the MPPT algorithm to control active power delivery to the grid. The power reference integrates virtual inertia and droop controls during an FS state, as presented in (7).

$$P_{ref} = P_{mppt} + P_{VIC} + P_D = P_{mppt} - 2H_{VIC}\frac{d\Delta f}{dt} - K_D\Delta f. \tag{7}$$

B. DC VIRTUAL INERTIA CONTROL

If power losses at converters are ignored, the voltage level at the DC capacitor reflects the power balance between RSC and GSC. However, any changes in system frequency do not impact the EE stored in the DC capacitor of PMSG-based WT. As a result, it is recommended that a DC capacitor
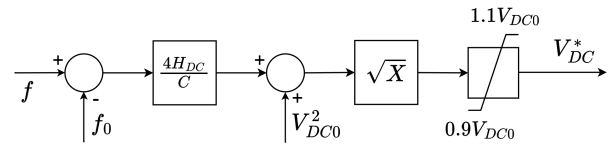
be linked with the system frequency to utilize its EE to participate in frequency support.

The dynamics of the DC-link voltage V_{DC} in per unit form can be written as [29] and [33]:

$$CV_{DC}\frac{dV_{DC}}{dt} = P_{in} - P_{out} = \Delta P_1. \tag{8}$$

$$C = \frac{C_{DC}V_{DC0}^2}{S_b}. \tag{9}$$

where S_B is the rated power of the WT, C_{DC} and C are the DC capacitance and the capacitance in p.u unit, respectively. V_{DC0} refers to the nominal voltage, P_{in} and P_{out} refer to the capacitor's input and output power, ΔP_1 refers to the power mismatch between P_{in} and P_{out}. In the following analysis, all the variables are in the per-unit form. The synchronous generator inertia response can be expressed as:

$$2H\frac{df}{dt} = P_m - P_e = \Delta P_2. \tag{10}$$

where H refers to the machine inertia time constant, f is the system frequency, P_m refers to the mechanical power, P_e is the electrical power, and ΔP_2 is the power mismatch between P_m and P_e. To mimic the inertia behavior of SG in (10), the power mismatch in the DC capacitor is assumed to equal the power mismatch between electrical and mechanical power at SG. The relationship between DC link voltage and system frequency can be determined as follows:

$$CV_{DC}\frac{dV_{DC}}{dt} = 2H\frac{df}{dt}. \tag{11}$$

where H_{DC} is the virtual inertia constant provided by the DC capacitor. Integrating two sides of (11) over time, the following equations can be obtained:

$$\int_{V_{DC0}}^{V_{DC}} CV_{DC}dV_{DC} = \int_{f_0}^{f} 2H_{DC}df. \tag{12}$$

$$\frac{C\left(V_{DC}^2 - V_{DC0}^2\right)}{2} = 2H_{DC}\left(f - f_0\right). \tag{13}$$

where f_0 and V_{DC0} are the nominal system frequency and nominal DC voltage, respectively. The maximum allowable DC voltage deviation in practice is ± 0.1 p.u [33], [35]. Therefore, this study set the limitation of DC voltage reference in the interval [0.9, 1.1] p.u. Based on (13), the DC voltage reference can be given in (14), and the control scheme of the DVIC strategy is illustrated in Fig. 4.

$$V_{DC} = \sqrt{\frac{4H_{DC}}{C}\Delta f + V_{DC0}^2}. \quad (14)$$

where $\Delta f = f - f_0$ is the range of frequency deviation covered by the DVIC strategy.

IV. PROPOSED STRATEGY FOR FREQUENCY REGULATION
This section introduces a novel approach for determining the adaptive DC coefficient H_{DC} using real-time voltage measurements. Furthermore, a coordinating control strategy adopting the new RS control approach will be discussed.

A. ADAPTIVE DC VIRTUAL INERTIA COEFFICIENT
Selecting an appropriate DC virtual coefficient H_{DC} is critical. Using a fixed coefficient H_{DC} in the DVIC algorithm makes the controller output depend only on frequency deviation instead of real-time DC voltage. In addition, if H_{DC} is less, the active power support from the DC capacitor cannot respond to a severe frequency event effectively. In contrast, if H_{DC} is large, a significant amount of active power will immediately be supplied to the grid, leading to a rapid depletion of energy in a DC capacitor. It might suddenly cause the DVIC controller's output to be set to zero.

To enhance the control performance of the DVIC strategy, this study proposes an adaptive DC coefficient H_{DC} following the real-time voltage at the DC bus. If the voltage gradually declines to $V_{DC,min} = 0.9$ p.u, it indicates that the DC capacitor has run out of energy storage. If the voltage at the DC bus gradually increases to $V_{DC,max} = 1.1$ p.u, the DC capacitor cannot absorb more energy. In addition, if the voltage moves to the upper or lower limits of the voltage operation interval [0.9, 1.1] p.u, $\frac{dV_{DC}}{dt}$ becomes zero. It indicates that the capacitor's ability to release (or absorb) energy has reached its limit. In contrast, if the voltage at the DC bus is close to the nominal $V_{DC0} = 1$ p.u, the DC capacitor has the potential to release (or absorb) a significant amount of energy to support frequency regulation. Thus, in this case, the setting of DC inertia coefficient H_{DC} should be large, and more power can be generated to support the grid. The detailed algorithm to adjust the DC inertia coefficient is listed as follows:

1) For the charging mode, if the DC voltage operates in the interval [0.9, 1) p.u, H_{DC} always equals $H_{DC,max}$. Once V_{DC} operates in the interval [1, 1.1] p.u, the equation to calculate the H_{DC} coefficient is changed to (15). Fig. 5(a) shows the relationship between H_{DC} and V_{DC} in the charging mode.
2) For discharging mode, if $V_{DC} < V_{DC0}$, it means the DC voltage operates in the interval [0.9, 1) p.u, then H_{DC}

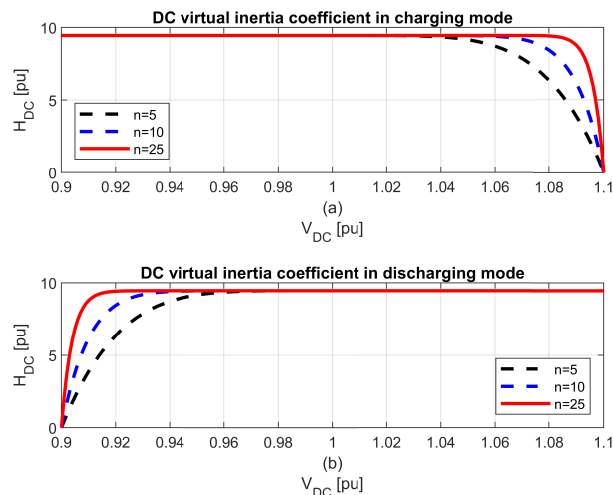**FIGURE 5.** DC virtual inertia coefficient H_{DC} with different *n*. (a) Charging mode. (b) Discharging modes.
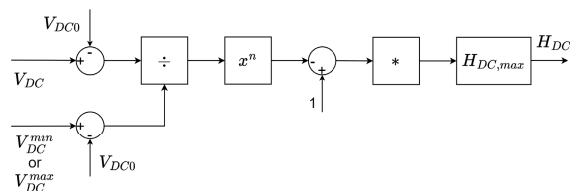

FIGURE 6. Block diagram of the adaptive DC virtual inertia control strategy.

is calculated according to (16). When V_{DC} operates in the interval [1, 1.1] p.u, H_{DC} equals $H_{DC,max}$. The relationship between H_{DC} and V_{DC} in the discharging mode is depicted in Fig. 5(b).

$$H_{DC} = H_{DC,max}\left[1 - \left(\frac{V_{DC} - V_{DC0}}{V_{DC,max} - V_{DC0}}\right)^n\right]. \quad (15)$$

$$H_{DC} = H_{DC,max}\left[1 - \left(\frac{V_{DC} - V_{DC0}}{V_{DC,min} - V_{DC0}}\right)^n\right]. \quad (16)$$

From (14), the inertia coefficient H_{DC} can be written by:

$$H_{DC} = \frac{C\left(V_{DC}^2 - V_{DC0}^2\right)}{4\Delta f}. \quad (17)$$

Generally, V_{DC} operates in the interval $\left[V_{DC,min}, V_{DC,max}\right]$. Before a disturbance occurs, DC voltage operates at $V_{DC0} = 1$ p.u nominally. Therefore, according to (17), it is obvious that the H_{DC} is the largest if $V_{DC} = V_{DC,max}$ at the maximum frequency deviation Δf_{max}. Thus, the range of inertia coefficient H_{DC} is determined by:

$$H_{DC} \leq \frac{C\left(V_{DC,max}^2 - V_{DC0}^2\right)}{4\Delta f_{max}}. \quad (18)$$

From (18), the maximum virtual inertia coefficient $H_{DC,max}$ can be given in (19).

$$H_{DC,max} = \frac{C\left(V_{DC,max}^2 - V_{DC0}^2\right)}{4\Delta f_{max}}. \quad (19)$$

Obviously, the value of n affects the H_{DC} value when V_{DC} is adjusted closely to the boundary point $V_{DC,max}$ or $V_{DC,min}$. If n is small, H_{DC} will gradually decrease when V_{DC} deviates from V_{DC0}. It will limit the output power from WTs. On the other hand, H_{DC} remains equal to $H_{DC,max}$ during the whole period for frequency support by the DVIC controller once n is large. Therefore, it may cause a sudden power drop as the same case at a fixed H_{DC}. To achieve a balance between active power production for frequency support and preventing abrupt power reductions to zero from the output of the DVIC controller, $n = 25$ was chosen in this study. The block diagram of the adaptive DC virtual inertia coefficient is illustrated in Fig. 6. When the DC voltage reaches its limit, the maximum frequency deviation $\Delta f_{max} = 0.01$ p.u, i.e., 0.6 Hz, is selected. Further, $V_{DC0} = 1$ p.u represents the DC voltage under normal operation, while $V_{DC,max} = 1.1$ p.u denotes the upper boundary voltage point. In this paper, the maximal virtual inertia coefficient $H_{DC,max} = 9.45$ is selected based on (19).

B. COORDINATED CONTROL STRATEGY

The cascading technique prioritizes DVIC as the initial use, followed by the frequency-based inertial control [33]. However, the energy loss remains significant while giving frequency regulation to the grid. The TFCC strategy was introduced in [34] to address the above problem. While this technique mitigates wind energy wastage, the magnitude of energy loss remains substantial. In the recovery process of WTs, the cascading or TFCC strategy exclusively relies on frequency information that neglects the use of rotor speed information. On the other hand, the rotor speed shows the mechanical characteristics of a WT. Therefore, this paper has proposed a novel control scheme that separates the WT operation into two distinct states: the FS and RS stages for WTs. This strategy utilizes the rotor speed derivative's negative-to-positive change to alter the operating mode from FS to RS. During the FS state, the WT maintains the power balance by providing frequency support. Once the FS process is completed, the WT must recover its rotor speed to the optimal operating state using the RS strategy.

In this paper, the FS strategy applies the TFCC proposed in [34] to combine the energy stored at the DC-link and KE in the WT to support frequency regulation. Its principle is given as follows:

1) After a frequency disturbance appears, the DVIC strategy immediately releases energy stored in the DC capacitor to participate in frequency support. The DC voltage reference in (14) is calculated by using the proposed adaptive DC coefficient H_{DC} in (15) and (16). If the frequency deviation exceeds $|\Delta f_{max}|$, it means that the capacitor's ability to release energy has reached its limit, while the system frequency remains reduced. Consequently, the KE stored in the rotating mass of WTs will be requested to contribute to the frequency support process.
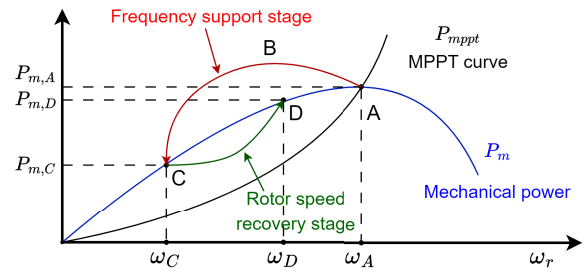

FIGURE 7. The dynamic response of the WT.

2) When the frequency-based inertia control strategy is activated, it sets the power reference to the sum of the total active power from the MPPT (P_{mppt}), additional power provided by virtual inertia (P_{VIC}) and droop control (P_D), as shown in (7).

Fig. 7 shows the active power of a WT during a FS state when a load suddenly increases. The WT is assumed to operate at the MPPT point A initially. The WT releases its KE to increase the active power following (7) to contribute to frequency support. The WT stops to support the additional power to the grid if the sign of the rotor speed derivative changes from negative to positive. This process is represented by a reduced rotor speed from ω_A to ω_C, corresponding to curve A-B-C. To avoid a significant drop in the rotor speed, the limit on $\omega_{r,min}$ should be considered in real operations. For the frequency-based inertia control strategy, the VIC method mainly impacts the initial short-term frequency when a disturbance occurs. Meanwhile, the droop method provides additional power when the frequency deviation increases. It is assumed that the secondary frequency control is not considered, the rotor speed of a WT will not recover to the initial value at ω_A, but it returns to ω_D, as shown in Fig. 7. It means the WT does not return to its initial MPPT operating point, causing wind energy loss after the WT supports frequency regulation. The cascading and TFCC strategies used a dead band to deactivate the droop strategy when the frequency deviation exceeds $|\Delta f_{max}|$. When applying these methods, the rotor speed can return to the initial value ω_A (see Fig. 7). However, a sudden deactivation of additional power would cause an oscillation at the output of WTs. Moreover, using only the frequency deviation as the input of the controller for rotor speed recovery cannot optimize the recovery process of the WT. For a given wind speed, (4) points out that each power curve has its maximum power point corresponding to a specific rotor speed. To maximize the available power from the wind, the rotor speed must be regulated to operate at the maximum power point. Therefore, the input of the RS controller should make the rotor speed of a WT return to its optimal operating point rapidly.

C. PROPOSED RS CONTROL STRATEGY

To enhance the efficiency of WT's operation after the FS stage and mitigate the oscillation problem, this paper proposed a novel strategy in the RS stage to enable the WT to recover its

rotor speed back to the initial value (ω_A). The RS controller is enabled after finishing the frequency-downward event if the sign of the rotor speed derivative is changed, as determined by:

$$P_{add} = \begin{cases} P_{FS}, & \text{if } \dfrac{d\omega_r}{dt} < 0 \\ P_{RS}, & \text{if } \dfrac{d\omega_r}{dt} > 0. \end{cases} \qquad (20)$$

where P_{add} denotes the additional power represented by P_{FS} during the FS and P_{RS} in the RS, respectively.

According to (20), the activation of either the FS or RS modes when the system frequency decreases depends on the sign of the derivative of rotor speed. The novel power command setting method for the WT during the RS state considers the power deviation between P_{mppt} and the mechanical power. It can be determined as follows:

$$P_{ref} = P_{mppt} - K_{RS}\left(P_m - P_{mppt}\right). \qquad (21)$$

where K_{RS} is a constant between 0 and 1. The value of K_{RS} can be set by:

$$K_{RS} = k\left[1 - \left(\frac{\omega_r - \omega_0}{\omega_{r,low} - \omega_0}\right)^m\right]. \qquad (22)$$

where ω_r is the rotor speed, ω_0 denotes the rotor speed at point A, $\omega_{r,low}$ is the lowest rotor speed at point C (it can be determined by the change of sign from negative to positive of the rotor speed derivative), k is the weight. To achieve a balance between the reduction of active power for RS and preventing abrupt significant power drop by WTs causing a second frequency dip, $k = 0.9$ was chosen for this work. Utilizing the RS strategy of (21)-(22), the power output of WTs will start from point C, then progressively approach to the MPPT curve, and eventually run stably at the initial operating point A. Thereby, the active power can be restored to the MPPT point after the frequency regulation of WTs. Fig. 8 illustrates the control method of the WT using its KE when it provides frequency support at the FS state. After completing the FS state, the RS control strategy subsequently adjusts the rotor speed to restore the WT to its optimal operating point. The slope limit controller $\frac{dP}{dt}$ limits the reduced power command value to prevent a sudden drop on the power reference P_{ref}, causing a second frequency dip when the RS controller activates. Compared with the cascading control and TFCC strategies, the advantages of the proposed strategy in this paper are summarized as follows:

1) The DVIC strategy adopts a novel adaptive H_{DC} coefficient to monitor the stored energy in capacitors and determine the appropriate output power for WTs.
2) Two operating stages are clearly distinguished as FS and RS states, corresponding to each controller for each stage. A novel power command setting with consideration of rotor speeds will be proposed. As a result, the proposed RS strategy reduces wind energy loss during the RS process. Moreover, it prevents the active power reference from suddenly returning to
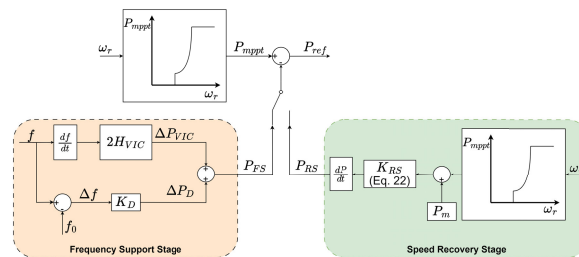

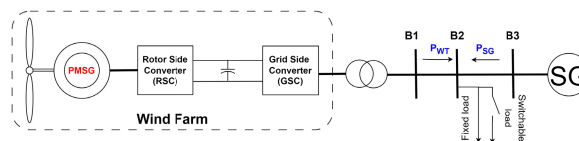**FIGURE 8.** The control algorithms of the FS and the RS strategies.

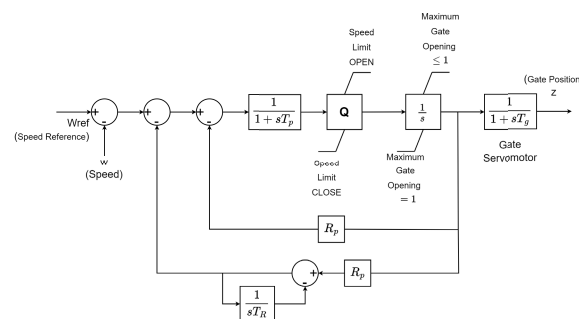**FIGURE 9.** Configuration of the simulation system.

FIGURE 10. The hydro-turbine governor model.

the MPPT operating point caused by disabling the frequency-based inertia controller.

V. SIMULATION

An appropriate power system based on PSCAD/EMTDC was established to evaluate the effectiveness of the proposed novel adaptive H_{DC} coefficient, only the DVIC strategy is used to participate in frequency regulation in Scenarios 1 and 2. Scenarios 3 to 5 will demonstrate the benefits of all suggested solutions under varying wind speed situations in this study. The test power system based on [26], [27], [28], [33], and [34] includes one 105 MW SG, one wind farm of 70 MW, a fixed load with 81 MW+8.1Mvar, and a switchable load with 8.1MW+0.81Mvar, as shown in Fig. 9. The hydro-turbine governor's block diagram and parameters are shown in Fig. 10 and Table 5 [42], [43]. The speed-governing with transient droop compensation, including permanent droop R_p, transient droop R_t, and reset time or dashpot time constant T_R are used for this SG model. In addition, T_p is the pilot valve and servo motor time constant, Q and T_g refer to servo gain and main servo time constant, respectively. The parameters of the test system are shown in Table 4 and 5 in the Appendix section. Three control strategies were used to validate the superiority of the proposed control strategy (Strategy 3), including two well-established methods: cascading strategy (Strategy 1) [33] and TFCC (Strategy 2) [34]. For the
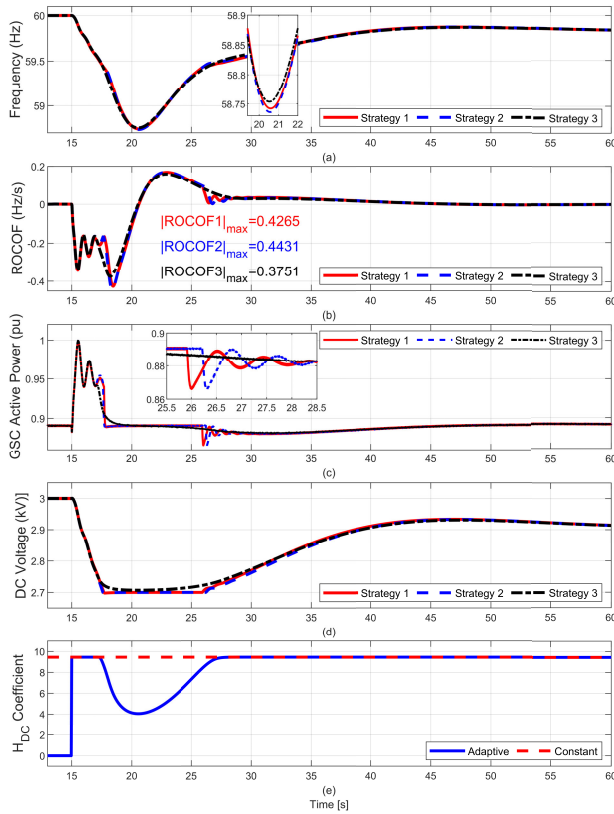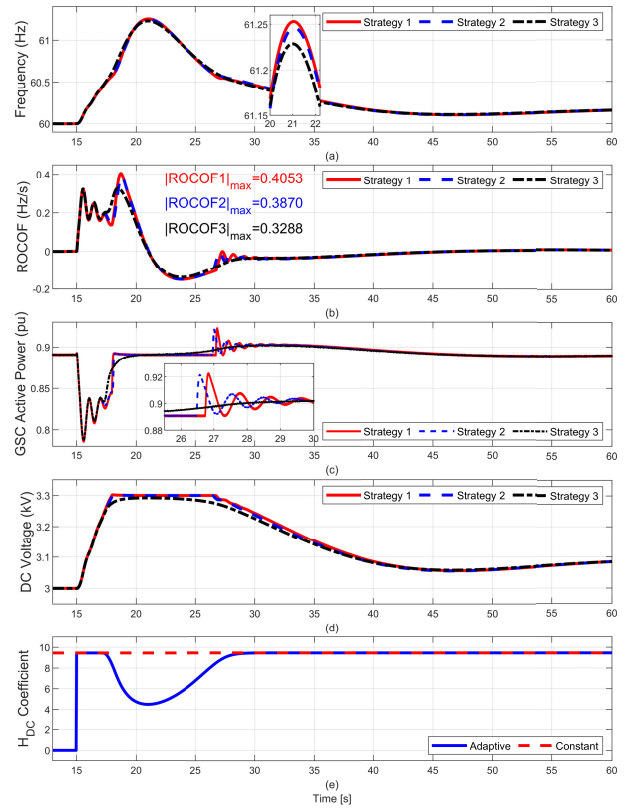
FIGURE 11. Simulation results of scenario 1. (a) System frequency. (b) ROCOF. (c) Power output from the WT. (d) DC-link voltage. (e) DC virtual inertia gain.

proposed method, the maximum virtual inertia coefficient for adaptive H_{DC} discussed in Section III is $H_{DC,max} = 9.45$. Additionally, the $K_{DC} = 10.5$ for the cascading strategy, and $H_{DC} = 9.45$ for the TFCC strategy. The droop coefficient in the cascading strategy is set to 6.5 to accomplish a similar frequency nadir by the TFCC and the proposed method. The DC virtual inertia coefficient is set to $H_{DC} = 3.2$ for three strategies.

A. SCENARIO 1: ONLY DC VIRTUAL INERTIA CONTROL PROVIDES FREQUENCY SUPPORT IN A CASE WITH A SUDDEN INCREASE ON LOAD

In this simulation, it is assumed that the wind speed is $v_\omega = 11.5$ m/s and a switchable load with 8.1MW+0.81Mvar (0.1 p.u) is connected at t = 15 s. This test is used to evaluate the performance of the proposed adaptive DVIC strategy.

Fig.11 presents the simulation results of Scenario 1. The system frequency using three strategies is shown in Fig.11(a), which verifies that the proposed strategy improves FN. Thus, the proposed method improves the frequency stability. Additionally, the proposed strategy also improves the performance of ROCOF, as shown in Fig.11(b), where the maximum $|ROCOF3|_{max} = 0.3751$ for Strategy 3 and highest $|ROCOF2|_{max} = 0.4431$ for Strategy 2. The FN and $|ROCOF|_{max}$ are summarized in Table 2. Fig. 11(c) plots the power output of the WT. At 17-18 s, the proposed method

FIGURE 12. Simulation results of scenario 2. (a) System frequency. (b) ROCOF. (c) Power output from the WT. (d) DC-link voltage. (e) DC virtual inertia gain.

**TABLE 2.** Frequency metrics for different cases.

Strategy	Frequency (Hz)		$|ROCOF|_{max}$ (Hz/s)	
	Scenario1	Scenario2	Scenario1	Scenario2
1	58.7421	61.2529	0.4265	0.4053
2	58.7359	61.2461	0.4431	0.3870
3	58.7536	61.2286	0.3751	0.3288

reduces the power output gradually to the MPPT reference value, but the strategies 1 and 2 cause a sudden drop on output power P_{GSC}. Moreover, the proposed adaptive method can avoid a power oscillation at 25-28 s when the frequency is recovered and the frequency deviation is less than $|\Delta f_{max}|$. The DC voltage is shown in Fig. 11(d). Fig. 11(e) depicts the curve of the DC virtual inertia gain by the three strategies during the transient period.

B. SCENARIO 2: ONLY DC VIRTUAL INERTIA CONTROL PROVIDING FREQUENCY SUPPORT ON SUDDEN LOAD DECREASE CASE

Fig. 12 depicts the simulation results when a 0.1 p.u sudden load is decreased by a switched load at 15 s. Scenario 2 investigates the performance of the proposed adaptive DVIC strategy, similar to the objectives of Scenario 1. As shown in Fig. 12(a), the FN by the proposed strategy is the lowest among all the strategies, demonstrating the reliability of the proposed adaptive algorithm. Fig. 12(b) shows that the
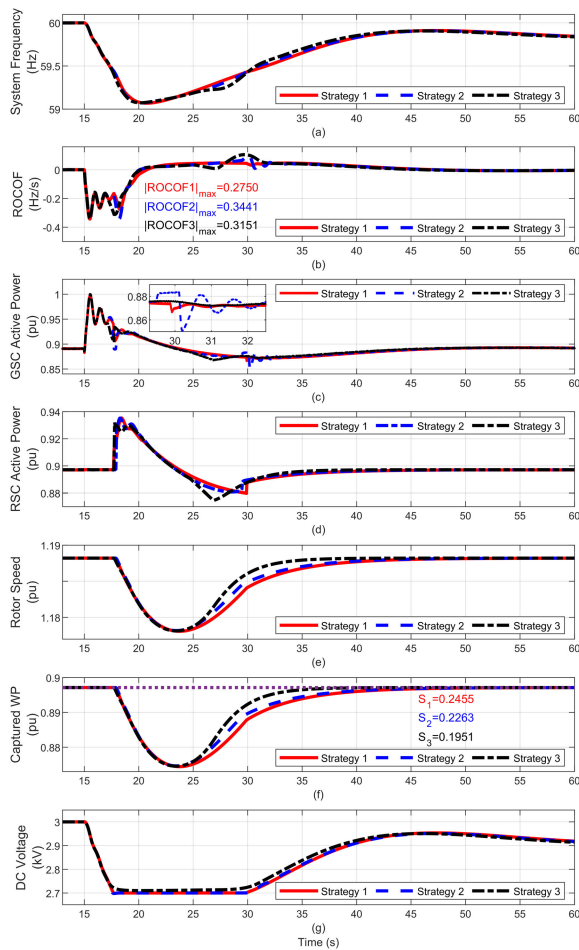
FIGURE 13. Simulation results of scenario 3. (a) System frequency. (b) ROCOF. (c) Power output from the GSC. (d) Power output from the RSC. (e) Rotor speed. (f) captured wind power. (g) DC-link voltage.

$|ROCOF|_{max}$ is improved obviously by the proposed method; the same simulation result can be obtained in Scenario 1. The detailed FN and $|ROCOF|_{max}$ are summarized in Table 2. Fig. 12(c) displays the power output of WTs. At 17-18 s, the proposed method increases the power output gradually, rather than raises it suddenly to the MPPT reference value. This result demonstrates that the proposed strategy obtains a better transient performance. Furthermore, when the frequency is recovered and the frequency deviation is less than $|\Delta f_{max}|$, power oscillation can be prevented by applying the proposed adaptive technique. Fig. 12(d) illustrates the voltage at the DC link. The curve of the DC virtual inertia gain by the three strategies is shown in Fig. 12(e). Using the adaptive technique, the DC virtual inertia gain varies based on the real time DC voltage instead of a constant value of 9.45 when applying the cascading and TFCC strategies.

C. SCENARIO 3: USING COORDINATED DC VIRTUAL INERTIA AND ROTOR VIRTUAL INERTIA STRATEGIES FOR FREQUENCY SUPPORT

This section demonstrates the advantages of the proposed strategy to distinguish FS and RS states. Fig.13 illustrates the

simulation results when a 0.1 p.u load is increased suddenly by inserting a load at 15 s with a wind speed of 11.5 m/s. In Scenarios 3, 4, and 5, both DVIC and frequency-based inertia strategies are considered. Based on the simulation results, the system frequency response and ROCOF are shown in Figs. 13(a) and (b), respectively. Fig. 13(g) displays the change of DC voltage when WTs participate in frequency regulation. It can be seen from Fig. 13(g) that the DC voltage gradually decreases and reaches its lowest allowable DC voltage between 15-18 s. It indicates the discharge of the EE stored in the DC capacitor. Once the DC capacitor achieves its maximum operational capacity of approximately 18 s, the RSC releases the kinetic energy stored in the spinning mass of WTs to participate in frequency control, as depicted in Fig. 13(d). The results point out that after releasing the rotational KE of WTs, the proposed RS strategy makes the power from RSC gradually decrease at 25-28 s, and the decreased power is greater compared to strategies 1 and 2. This will support a fast rotor-speed recovery, as shown in Fig. 13(e). Therefore, the proposed strategy obtains better performance in recovering rotor speeds and then reduces wind energy loss. Fig. 13(f) shows that the wind energy loss by the cascading, TFCC, and proposed strategies are $S_1 = 0.2455$ p.u, $S_2 = 0.2263$ p.u, and $S_3 = 0.1951$ p.u, respectively. The wind energy loss by each control strategy is summarized in Table 3. Compared with the cascading and the TFCC methods, the energy loss by the proposed method is reduced by 20.52 % and 14.78 % per WT, respectively. Fig. 13(c) illustrates the power output from the GSC. Around 29-32s, strategies 1 and 2 cause a fluctuating power generation. That is, once the quasi-steady-state frequency deviation is within the deadband $|\Delta f_{max}|$, WTs by the control strategy 1 or 2 automatically return to their MPPT operating points. However, the proposed strategy can avoid such a problem, which makes the power generation smoother.

D. SCENARIO 4: USING COORDINATED DC VIRTUAL INERTIA AND ROTOR VIRTUAL INERTIA STRATEGIES FOR FREQUENCY SUPPORT

Fig. 14 shows the simulation results when a 0.1 p.u load is increase suddenly by inserting a load at 15 s with a wind speed of 10 m/s. The system frequency response and ROCOF are shown in Figs. 14(a) and (b), respectively. As shown in Fig. 14(g), the varying DC voltage from its nominal to its lowest operation point participates in frequency regulation in about 15-18 s. The reduction in DC voltage represents the DC capacitor releasing the electrostatic energy. Once the DC capacitor reaches its entire working capacity of around 18 s, the RSC releases the kinetic energy held in the rotating mass of WTs to contribute to frequency regulation, as shown in Fig. 14(d). The outcomes indicate that the power from RSC decreases progressively at 25-28 s when the proposed RS strategy is implemented. Furthermore, the power reduction is more significant compared to strategies 1 and 2. It will support a fast rotor speed recovery, as shown
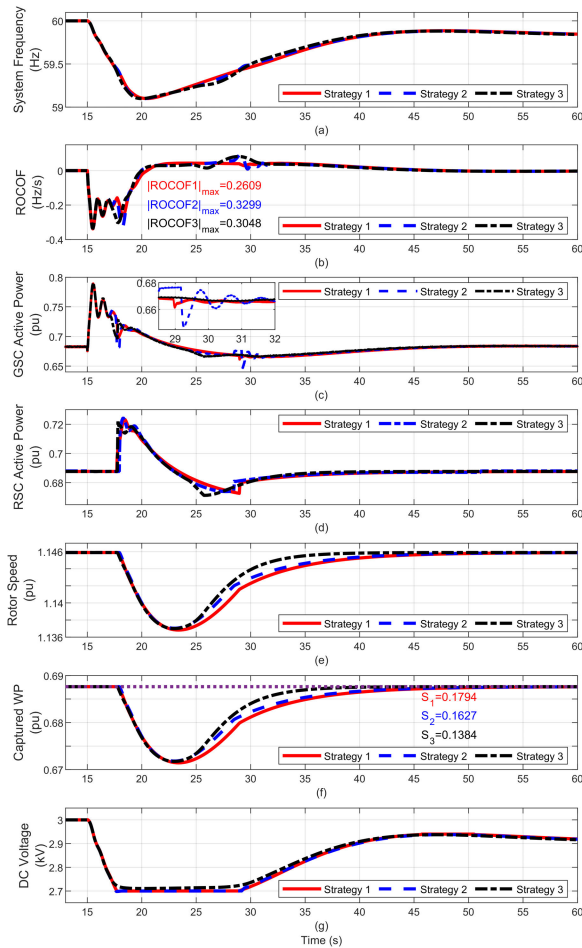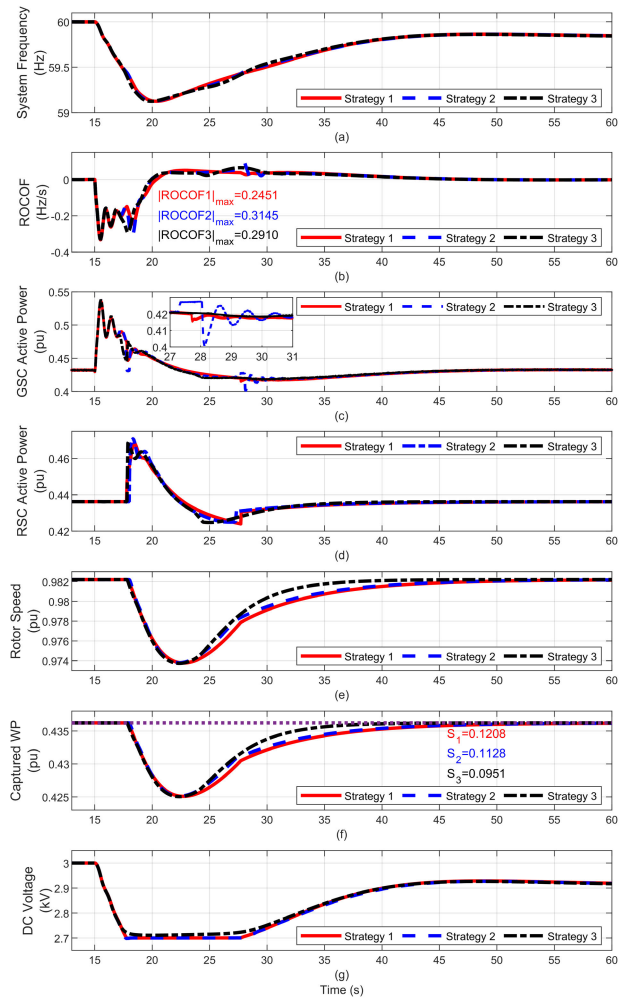
FIGURE 14. Simulation results of scenario 4. (a) System frequency. (b) ROCOF. (c) Power output from the GSC. (d) Power output from the RSC. (e) Rotor speed. (f) captured wind power. (g) DC-link voltage.

in Fig. 14(e). Therefore, the proposed strategy has a better performance on the recovery of rotor speeds, which reduces wind energy loss. Fig. 14(f) illustrates that the wind energy loss by the cascading, TFCC, and proposed strategies are $S_1 = 0.1794$ p.u, $S_2 = 0.1627$ p.u, and $S_3 = 0.1384$ p.u, respectively. Compared with the cascading and TFCC methods, the energy loss by the proposed method is reduced by 22.85 % and 14.94 % per WT, respectively. The results show that the proposed strategy captures more wind than the cascading or TFCC strategy, while the three strategies cause the same frequency nadir across a range of wind speeds. The adaptive strategy ensures smooth output power of the DVIC controller, as shown in Fig. 14(c). Around 29-32s, strategies 1 and 2 cause a fluctuate power generation. However, the proposed strategy can avoid such a problem, which makes the power generation more smooth.

E. SCENARIO 5: USING COORDINATED DC VIRTUAL INERTIA AND ROTOR VIRTUAL INERTIA STRATEGIES FOR FREQUENCY SUPPORT

Fig. 15 illustrates the simulation results when a 0.1 p.u load is increased suddenly by adding a load at 15 s with

FIGURE 15. Simulation results of scenario 5. (a) System frequency. (b) ROCOF. (c) Power output from the GSC. (d) Power output from the RSC. (e) Rotor speed. (f) captured wind power. (g) DC-link voltage.

TABLE 3. Wind energy loss.

Strategy	Wind Energy Loss (p.u)		
	Scenario 3	Scenario 4	Scenario 5
1	0.2455	0.1794	0.1208
2	0.2455	0.1794	0.1208
3	0.1951	0.1384	0.0951

a wind speed of 8 m/s. Figs. 15(a) and (b) show the system frequency response and ROCOF, respectively. The DC voltage gradually decreases and eventually reaches its lowest point at approximately 18 s, as denoted in Fig. 15(g). During this process, the energy stored in the DC capacitor is released. Once the DC capacitor is fully discharged (around 18 seconds), the RSC taps into the kinetic energy stored in the rotating mass of WTs, contributing to frequency regulation, as shown in Fig. 15(d). Furthermore, by releasing the KE of WTs, the power generated from the RSC decreases progressively at 25-27 s using the proposed RS strategy, which is significantly greater than strategies 1 and 2. It will accelerate the recovery of rotor speed, as shown in Fig. 15(e).

TABLE 4. Parameter of PMSG-based WT.

Item	Value
Rated power	2 MW
Nominal frequency	60 Hz
Rated DC-link voltage	3 kV
DC-link Capacitance	0.1 F
Inertia Constant	4 s
Terminal Voltage	690 V
Rated Wind Speed	12 m/s
Rated Rotor Speed	1.2 p.u
Cut in Wind Speed	5 m/s
Cut Out Wind Speed	20 m/s

TABLE 5. Parameters of SG.

Item	Value
Rated Power	105 MW
Terminal Voltage	6.6 kV
Inertia Time Constant	3.2 s
x_d, x_d', x_d''	1.305, 0.296, 0.252
x_q, x_q'', x_l	0.474, 0.243, 0.18
T_{d0}, T_{d0}', T_{q0}'	1.01, 0.053, 0.071
Permanent droop Rp	0.04 pu
Temporary droop Rt	0.4
Reset time TR	5 s
Servomotor time constant Tp	0.05 s
Servo gain Q	5
Main servo time constant T_g	0.2 s
Maximum gate opening	1
Minimum gate	0
Speed limit open	0.04 pu/s
Speed limit close	0.04 pu/s

Hence, the proposed strategy has better performance of recovery rotor speed, which reduces wind energy loss. Fig. 15(f) shows that the wind energy loss by the cascading, TFCC, and proposed strategies are $S_1 = 0.1208$ p.u, $S_2 = 0.1128$ p.u, and $S_3 = 0.0951$ p.u, respectively. Compared with the cascading and TFCC methods, the energy loss by the proposed method is reduced by 21.27 % and 15.69 % per WT. The adaptive strategy guarantees a smooth power output from the DC-link virtual inertial controller, as illustrated in Fig. 15(c). Around 29-32s, Strategies 1 and 2 cause a fluctuate power generation. However, the proposed strategy can avoid such a problem, which makes the power generation more smooth.

VI. CONCLUSION

This paper proposes a novel adaptive DC virtual inertia coefficient that makes the active power from GSC change smoothly. Moreover, compared to previous works, the new RS control strategy performs better in reducing the loss of wind power. This has been proven through the simulation results of this paper. Under different wind speed scenarios, the proposed method reduces energy loss by approximately 21% and 15% compared to the cascading and TFCC strategies, respectively. In addition, the new RS control strategy can prevent the power reference value from returning to the MPPT point of WTs when the quasi-steady-state frequency deviation falls into the deadband. The main contributions of this paper are summarized as follows:

1) This paper designs an adaptive DC virtual inertia coefficient following the real-time DC voltage. The proposed method can adjust the controller's output smoothly, preventing a sudden change on active power due to the depletion of energy in a DC-link capacitor.

2) This paper proposed a new control strategy for the RS state, which obtains a better performance on capturing wind energy.

However, given a widespread integration of renewable energy sources (RES) into the power system, RES must play a more active role in ensuring system stability. Therefore, our future research will focus on examining the grid-forming capabilities of WTs and conducting a comparative analysis with the proposed method to assess its effectiveness. In addition, a comprehensive strategy integrated with other RE sources, batteries, and supercapacitors will be implemented to evaluate the dynamic frequency response in the context of high penetration of RES in the power grid.

APPENDIX
See Tables 4 and 5.

REFERENCES

[1] D. Kumar and K. Chatterjee, "A review of conventional and advanced MPPT algorithms for wind energy systems," *Renew. Sustain. Energy Rev.*, vol. 55, pp. 957–970, Mar. 2016.

[2] C.-H. Lin and Y.-K. Wu, "Coordinated frequency control strategy for VSC-HVDC-connected wind farm and battery energy storage system," *IEEE Trans. Ind. Appl.*, vol. 59, no. 5, pp. 5314–5328, Sep./Oct. 2023.

[3] M. Mehrabankhomartash, M. Saeedifard, and A. Yazdani, "Adjustable wind farm frequency support through multi-terminal HVDC grids," *IEEE Trans. Sustain. Energy*, vol. 12, no. 2, pp. 1461–1472, Apr. 2021.

[4] Y.-L. Hu and Y.-K. Wu, "Inertial response identification algorithm for the development of dynamic equivalent model of DFIG-based wind power plant," *IEEE Trans. Ind. Appl.*, vol. 57, no. 3, pp. 2104–2113, May 2021.

[5] Y. Cheng, R. Azizipanah-Abarghooee, S. Azizi, L. Ding, and V. Terzija, "Smart frequency control in low inertia energy systems based on frequency response techniques: A review," *Appl. Energy*, vol. 279, Dec. 2020, Art. no. 115798.

[6] H. Liu, M. Li, L. Liu, and J. Shi, "Frequency trajectory planning-based transient frequency regulation strategy for wind turbine systems," *IEEE J. Emerg. Sel. Topics Power Electron.*, vol. 10, no. 4, pp. 3987–4000, Aug. 2022.

[7] H. Liu and C. Liu, "Frequency regulation of VSC-MTDC system with offshore wind farms," *IEEE J. Emerg. Sel. Topics Power Electron.*, vol. 12, no. 1, pp. 275–286, Jan. 2024.

[8] H. Lao, L. Zhang, T. Zhao, and L. Zou, "Innovated inertia control of DFIG with dynamic rotor speed recovery," *CSEE J. Power Energy Syst.*, vol. 8, no. 5, pp. 1417–1427, Sep. 2022.

[9] K. V. Vidyanandan and N. Senroy, "Primary frequency regulation by deloaded wind turbines using variable droop," *IEEE Trans. Power Syst.*, vol. 28, no. 2, pp. 837–846, May 2013.

[10] S. Wang, J. Hu, X. Yuan, and L. Sun, "On inertial dynamics of virtual-synchronous-controlled DFIG-based wind turbines," *IEEE Trans. Energy Convers.*, vol. 30, no. 4, pp. 1691–1702, Dec. 2015.

[11] D. Yang, J. Kim, Y. C. Kang, E. Muljadi, N. Zhang, J. Hong, S.-H. Song, and T. Zheng, "Temporary frequency support of a DFIG for high wind power penetration," *IEEE Trans. Power Syst.*, vol. 33, no. 3, pp. 3428–3437, May 2018.

[12] M. Kang, E. Muljadi, K. Hur, and Y. C. Kang, "Stable adaptive inertial control of a doubly-fed induction generator," *IEEE Trans. Smart Grid*, vol. 7, no. 6, pp. 2971–2979, Nov. 2016.

[13] M. Kheshti, S. Lin, X. Zhao, L. Ding, M. Yin, and V. Terzija, "Gaussian distribution-based inertial control of wind turbine generators for fast frequency response in low inertia systems," *IEEE Trans. Sustain. Energy*, vol. 13, no. 3, pp. 1641–1653, Jul. 2022.

[14] M. Kang, K. Kim, E. Muljadi, J.-W. Park, and Y. C. Kang, "Frequency control support of a doubly-fed induction generator based on the torque limit," *IEEE Trans. Power Syst.*, vol. 31, no. 6, pp. 4575–4583, Nov. 2016.

[15] N. R. Ullah, T. Thiringer, and D. Karlsson, "Temporary primary frequency control support by variable speed wind turbines—Potential and applications," *IEEE Trans. Power Syst.*, vol. 23, no. 2, pp. 601–612, May 2008.

[16] A. D. Hansen, M. Altin, I. D. Margaris, F. Iov, and G. C. Tarnowski, "Analysis of the short-term overproduction capability of variable speed wind turbines," *Renew. Energy*, vol. 68, pp. 326–336, Aug. 2014.

[17] F. Hafiz and A. Abdennour, "Optimal use of kinetic energy for the inertial support from variable speed wind turbines," *Renew. Energy*, vol. 80, pp. 629–643, Aug. 2015.

[18] S. El Itani, U. D. Annakkage, and G. Joos, "Short-term frequency support utilizing inertial response of DFIG wind turbines," in *Proc. IEEE Power Energy Soc. Gen. Meeting*, Jul. 2011, pp. 1–8.

[19] M. Kang, J. Lee, and Y. C. Kang, "Modified stepwise inertial control using the mechanical input and electrical output curves of a doubly fed induction generator," in *Proc. 9th Int. Conf. Power Electron.*, 2015, pp. 357–361.

[20] G. C. Tarnowski, P. C. Kjar, P. E. Sorensen, and J. Ostergaard, "Variable speed wind turbines capability for temporary over-production," in *Proc. IEEE Power Energy Soc. Gen. Meeting*, Jul. 2009, pp. 1–7.

[21] C.-H. Lin and Y.-K. Wu, "Overview of frequency-control technologies for a VSC-HVDC-Integrated wind farm," *IEEE Access*, vol. 9, pp. 112893–112921, 2021.

[22] J. Morren, S. W. H. de Haan, W. L. Kling, and J. A. Ferreira, "Wind turbines emulating inertia and supporting primary frequency control," *IEEE Trans. Power Syst.*, vol. 21, no. 1, pp. 433–434, Feb. 2006.

[23] M. Hwang, E. Muljadi, G. Jang, and Y. C. Kang, "Disturbance-adaptive short-term frequency support of a DFIG associated with the variable gain based on the ROCOF and rotor speed," *IEEE Trans. Power Syst.*, vol. 32, no. 3, pp. 1873–1881, May 2017.

[24] M. Altin, A. D. Hansen, T. K. Barlas, K. Das, and J. N. Sakamuri, "Optimization of short-term overproduction response of variable speed wind turbines," *IEEE Trans. Sustain. Energy*, vol. 9, no. 4, pp. 1732–1739, Oct. 2018.

[25] Y.-K. Wu, W.-H. Yang, Y.-L. Hu, and P. Q. Dzung, "Frequency regulation at a wind farm using time-varying inertia and droop controls," *IEEE Trans. Ind. Appl.*, vol. 55, no. 1, pp. 213–224, Jan. 2019.

[26] C. Pradhan, C. N. Bhende, and A. K. Samanta, "Adaptive virtual inertia-based frequency regulation in wind power systems," *Renew. Energy*, vol. 115, pp. 558–574, Jan. 2018.

[27] X. Zeng, T. Liu, S. Wang, Y. Dong, and Z. Chen, "Comprehensive coordinated control strategy of PMSG-based wind turbine for providing frequency regulation services," *IEEE Access*, vol. 7, pp. 63944–63953, 2019.

[28] J. Zhu, J. Hu, W. Hung, C. Wang, X. Zhang, S. Bu, Q. Li, H. Urdal, and C. D. Booth, "Synthetic inertia control strategy for doubly fed induction generator wind turbine generators using lithium-ion supercapacitors," *IEEE Trans. Energy Convers.*, vol. 33, no. 2, pp. 773–783, Jun. 2018.

[29] M. F. M. Arani and E. F. El-Saadany, "Implementing virtual inertia in DFIG-based wind power generation," *IEEE Trans. Power Syst.*, vol. 28, no. 2, pp. 1373–1384, May 2013.

[30] L. Chen and F. Blaabjerg, "Virtual synchronous generator based on type-IV wind turbine with supercapacitor as storage," in *Proc. IEEE/IAS Ind. Commercial Power Syst. Asia*, Jul. 2021, pp. 1194–1200.

[31] X. Zeng, X. Li, S. Wang, T. Liu, C. Zhang, and H. Zhang, "Virtual inertia control and short-term primary control for PMSG-based wind turbine using supercapcitor," in *Proc. 4th Int. Conf. HVDC (HVDC)*, Nov. 2020, pp. 191–196.

[32] X. Liu, Z. Xu, and J. Zhao, "Combined primary frequency control strategy of permanent magnet synchronous generator-based wind turbine," *Electric Power Compon. Syst.*, vol. 46, nos. 14–15, pp. 1704–1718, Sep. 2018.

[33] Y. Li, Z. Xu, and K. P. Wong, "Advanced control strategies of PMSG-based wind turbines for system inertia support," *IEEE Trans. Power Syst.*, vol. 32, no. 4, pp. 3027–3037, Jul. 2017.

[34] Q. Jiang, X. Zeng, B. Li, S. Wang, T. Liu, Z. Chen, T. Wang, and M. Zhang, "Time-sharing frequency coordinated control strategy for PMSG-based wind turbine," *IEEE J. Emerg. Sel. Topics Circuits Syst.*, vol. 12, no. 1, pp. 268–278, Mar. 2022.

[35] M. F. M. Arani and Y. A. I. Mohamed, "Assessment and enhancement of a full-scale PMSG-based wind power generator performance under faults," *IEEE Trans. Energy Convers.*, vol. 31, no. 2, pp. 728–739, Jun. 2016.

[36] H. Shutari, N. Saad, N. B. M. Nor, M. F. N. Tajuddin, A. Alqushaibi, and M. A. Magzoub, "Towards enhancing the performance of grid-tied VSWT via adopting sine cosine algorithm-based optimal control scheme," *IEEE Access*, vol. 9, pp. 139074–139088, 2021.

[37] A. Yazdani and R. Iravani, *Voltage-Sourced Converters in Power Systems: Modeling, Control, and Applications*. Hoboken, NJ, USA: Wiley, 2010.

[38] H. Shutari, T. Ibrahim, N. B. M. Nor, H. Q. A. Abdulrab, N. Saad, and Q. Al-Tashi, "Coordination of enhanced control schemes for optimal operation and ancillary services of grid-tied VSWT system," *IEEE Access*, vol. 11, pp. 43520–43535, 2023.

[39] Y. Xia, K. H. Ahmed, and B. W. Williams, "Wind turbine power coefficient analysis of a new maximum power point tracking technique," *IEEE Trans. Ind. Electron.*, vol. 60, no. 3, pp. 1122–1132, Mar. 2013.

[40] G. Abad, J. Lopez, M. Rodriguez, L. Marroyo, and G. Iwanski, *Doubly Fed Induction Machine: Modeling and Control for Wind Energy Generation*. Hoboken, NJ, USA: Wiley, 2011.

[41] H. Shutari, T. Ibrahim, N. B. Mohd Nor, N. Saad, M. F. N. Tajuddin, and H. Q. A. Abdulrab, "Development of a novel efficient maximum power extraction technique for grid-tied VSWT system," *IEEE Access*, vol. 10, pp. 101922–101935, 2022.

[42] W. Group Prime Mover and E. Supply, "Hydraulic turbine and turbine control models for system dynamic studies," *IEEE Trans. Power Syst.*, vol. 7, no. 1, pp. 167–179, Feb. 1992.

[43] P. Kundur, *Power System Stability and Control*. New York, NY, USA: McGraw-Hill, 1994.

DUC-TUNG TRINH (Graduate Student Member, IEEE) received the B.S. degree in electrical engineering from Hanoi University of Science and Technology (HUST), Vietnam, in 2021. He is currently pursuing the M.S. degree with the National Chung Cheng University.

His research interests include inverter-based resources grid-forming, wind turbine modeling, and control.

YUAN-KANG WU (Member, IEEE) received the Ph.D. degree in electronic and electrical engineering from the University of Strathclyde, Glasgow, U.K., in 2004.

He was a Researcher at the Industrial Technology Research Institute, Hsinchu, Taiwan, and an Engineer at the Taiwan Electric Research and Testing Center, Taiwan. He is currently a Professor with the Department of Electrical Engineering, National Chung Cheng University, Chiayi City, Taiwan, working in the area of wind turbine modeling, wind and solar power systems, offshore wind farm planning, renewable energy forecasting techniques, power system control and management, distributed generation, and smart grid control. He is also the Technical Committee Program Chair of Energy Systems Committee of Industry Application Society of IEEE and an Associate Editor of IEEE Transactions on Industry Applications.

MANH-HAI PHAM (Member, IEEE) was born in Hai Duong, Vietnam, in 1983. He received the B.S. degree in power system from Hanoi University of Science and Technology, in 2006, the M.S. degree in power system from the University of Paul Sabatiers, Toulouse, France, in 2008, and the Ph.D. degree in plasma applications from the University of Poitiers, Poitiers, France, in 2011.

Since 2012, he has been a Lecturer with Electrical Power University, Hanoi, Vietnam. His research interests include nonthermal plasma discharge processes and applications, load forecasting, reliability of power systems, and renewable energy.